

Accepted Manuscript

Highly oxygen deficient, bimodal mesoporous silica based supercapacitor with enhanced charge storage characteristics

Akanksha Joshi, Shubra Lalwani, Gurmeet Singh, Raj Kishore Sharma



PII: S0013-4686(18)32731-2

DOI: <https://doi.org/10.1016/j.electacta.2018.12.033>

Reference: EA 33248

To appear in: *Electrochimica Acta*

Received Date: 12 August 2018

Revised Date: 13 November 2018

Accepted Date: 4 December 2018

Please cite this article as: A. Joshi, S. Lalwani, G. Singh, R.K. Sharma, Highly oxygen deficient, bimodal mesoporous silica based supercapacitor with enhanced charge storage characteristics, *Electrochimica Acta* (2019), doi: <https://doi.org/10.1016/j.electacta.2018.12.033>.

This is a PDF file of an unedited manuscript that has been accepted for publication. As a service to our customers we are providing this early version of the manuscript. The manuscript will undergo copyediting, typesetting, and review of the resulting proof before it is published in its final form. Please note that during the production process errors may be discovered which could affect the content, and all legal disclaimers that apply to the journal pertain.

Highly Oxygen Deficient, Bimodal Mesoporous Silica based Supercapacitor with enhanced Charge Storage Characteristics

Akanksha Joshi, Shubra Lalwani, Gurmeet Singh* and Raj Kishore Sharma**

Department of Chemistry, University of Delhi, Delhi-110007, INDIA

Abstract

The present study elaborates facile approach to generate active sites in cashew nut shaped silica (SiO_2). These active sites are attributed to the high concentration of oxygen vacancies and bimodal mesoporosity in silica owing to etching and calcination treatment. In the etched calcined silica (ECS), mesopores act as buffered spaces, whereas, OVs provide high carrier/donor density ($3 \times 10^{24} \text{cm}^{-3}$). High density of carriers/donor reduces the distance between active sites (2.5 nm) further enhancing the rate of electron transfer. Consequent to the unique combination of OVs and bimodal mesoporosity, ECS exhibits high electrochemically accessible surface area ($3170 \text{ m}^2 \text{ g}^{-1}$) and excellent charge storage in ECS||ECS cell ($\sim 337 \text{ F g}^{-1}$ at 1 A g^{-1}). In addition, the symmetric cell (ECS||ECS) delivers maximum energy density of 46.86 Wh Kg^{-1} at power density of 537.59 W Kg^{-1} with respectable capacitance retention (111 % after 10,000 cycles). Remarkably, the solid state flexible device unveiled energy density of 2.16 Wh Kg^{-1} at 166.05 W Kg^{-1} even under the bent state retaining 165 % of its capacitance up till 3000 cycles. This work essentially highlights the synergism between mesoporosity and oxygen vacancies on the charge storage characteristics of silica.

Abbreviations: as-synthesized silica (AS), etched silica (ES), etched calcined silica (ECS), oxygen vacancies (OVs)

Keywords: Cashew nut shaped silica, Oxygen Vacancies, Bimodal mesoporous, Supercapacitor, Carrier/donor density

****Corresponding author:** Raj K. Sharma (drrajksharma@yahoo.co.in)

***Co-corresponding author:** Gurmeet Singh (gurmeet123@yahoo.co.in)

Tel. No.:+91-11-27666616

Research highlights

- High carrier/donor density ($3 \times 10^{24} \text{ cm}^{-3}$) in oxygen deficient cashew nut shape silica.
- Minimal distance (2.5 nm) between active sites ameliorates the current density.
- Bimodal mesoporosity and OV's endows cashew nut shape silica with high specific capacitance of 337 F g^{-1} at 1 A g^{-1} .
- Flexible solid state device exhibits good capacitive behaviour even in deformed state.

1. Introduction

The alarming issues of environment [1,2] and clean energy demand have triggered researchers towards designing advanced green energy storage devices. Supercapacitors (SCs), a new class of energy storage devices, meet the demands of advanced applications requiring high power delivery [3]. SCs have been considered as eco-friendly energy storage devices with commendable features like high power density, fast charge–discharge characteristics, peak operating voltage, long cycle life and reliability [4–7].

In order to realize good performance, there should be a balance between specific surface area and conductivity of the material. Use of porous/large surface area materials is one of the key approach for shortening the diffusion pathway of electrolytic ions. To enhance charge/discharge rate, several conductive agents are incorporated into electrode material [8,9]. However, effective volume density of the electro-active material decreases by addition of conductive agents [10]. Thus, to boost the conductivity as well as porosity, modification in

composition and structure of the electrode material is a wise strategy. Silicon, a semiconducting material [11] has recently gathered attention in the area of energy storage due to its high abundance in earth crust, easy availability, minimal environmental impact, high thermal stability [12] and unique electronic and chemical properties. Porous silica (derivative of silicon) offers desirable properties such as high surface area, low toxicity [13], high differential capacitance (upto $180 \mu\text{F cm}^{-2}$) [14], hydrophilicity [15], and excellent chemical stability [16] enduring harsh environments like high temperature and strong acids/bases. Although silica has been explored in Li ion batteries [17–19], but the studies on utilization of silicon [20–23] and porous silica [24–28] as an electrode in supercapacitors are lacking. A vast array of morphologies [29–32] and the presence of large number of hydrophilic surface groups (e.g. OH) [33,34] make silica appealing as an energy storage material. In earlier studies, improvement in capacitance of carbon electrodes using SiO_2 nanoparticle [35] as fillers has also been reported by Leonard *et al.* Other reports in continuation endorse the role of silica particles in polyaniline matrix in achieving better cycling stability [36]. Even though there are numerous advantages associated with silica, yet low electronic conductivity [37] i.e. its insulating nature (wide band gap) limits its application as a capacitive electrode. Hence, it is extremely desirable to improve the conductivity of silica electrode. To eliminate this issue, we have introduced intrinsic defects into the structure of silica. Electrochemical and electronic properties of metal oxides are strongly influenced by the intrinsic defects [38,39]. Introduction of oxygen vacancies (OVs), one of the intrinsic defects is considered as an n-type dopant. These dopants improve the kinetics of charge storage and conductivity of the material by shifting Fermi level close to the conduction band [40]. Since, the formation energy of oxygen vacancy is small, it can be easily introduced as anion vacancy into the metal oxide [41].

Different from previous studies, here silica is synthesized in cashew nut shaped morphology. This morphology provides more active edge sites for the participation in redox reactions. To further obtain the porosity in ionic accessible range, etching is carried out. Generally, etching deals at high temperature using corrosive and hazardous etchants (e.g. HF) [42]. We have adopted etching based on the spontaneous dissolution and regrowth of silica using NaBH_4 (etching agent) and PVP (surface protecting agent) [43]. The abovementioned process does not require harsh conditions and can be performed in the absence of inert atmosphere, thus turning out to be completely facile, green and economical. Interestingly oxygen vacancies (OVs) with the aid of NaBH_4 were introduced on the surface accompanied large size mesopores. Mesoporous structure helps in providing a large accessible surface area for ion transport/charge storage and also act as a buffering reservoirs [44–46] whereas oxygen vacancies (OVs) build the localized states below the conduction band so that valence band can easily overlap with the conduction band [47]. This in turn improves the conductivity of silica with enhancement in the active sites for redox reactions. Further, calcination treatment enriched the silica with small size mesopores. Thus, the final product exhibits bimodal mesoporosity with ample amount of oxygen vacant sites. Bimodal porosity is shown to have significant role in improving the ion-transport kinetics [48] as it increases the electrochemically active surface area of the silica by nearly four times than the BET surface area. In the present study, we have elucidated the synergistic effect of bimodal porosity and oxygen vacancy on the electrochemical performance of silica electrodes. Oxygen deficiency in silica results in a huge improvement in number of carrier/donor densities that in turn increases the rate of electron transfer. The deduction of oxygen from the SiO_2 structure generates enormous free electrons that direct to the transition in behaviour from insulating to semiconductive [49]. This also lessen the potential barrier exist in between Fermi level of silica electrode and redox potential of electrolyte [50]. The oxygen deficient mesoporous

cashew nut shaped silica electrodes acquires maximum energy density of 46.86 Wh Kg⁻¹ at power density of 537.59 W Kg⁻¹. The mesoporosity in the structure helps to attain excellent cycling stability upto 10000 cycles by acting as buffered spaces. For portable application, a solid state and flexible device is much needed. Here, we have fabricated flexible solid state device to meet the growing demands of wearable and miniaturized electronic devices. The assembled flexible solid state device shows a very little change in the capacitive behaviour under normal to bend conditions and exhibiting energy density of 2.16 Wh Kg⁻¹ at 166.05 W Kg⁻¹. The uniqueness of our work is the utilization of facile and economical method in development of silica as a charge storage material by using synergism of mesoporosity and oxygen deficiency. The above characteristics motivate to explore silica as an alternative to carbon and metal oxide in the development of flexible, light weight and environment friendly supercapacitor. To the best of our knowledge, no such work based on the Oxygen deficient and bimodal mesoporous silica as a charge storage material with such high electrochemical performance has been reported so far.

2. Experimental section

2.1. *Synthesis of SiO₂*

SiO₂ was prepared by a surfactant assisted sol-gel method in a Stober's solution. The molar ratio of the TEOS (tetra ethyl orthosilicate): CTAB (cetyl trimethyl ammonium bromide): NH₃ (aq. ammonia): C₂H₅OH (ethyl alcohol): H₂O reaction mixture was 1.0: 0.38: 4.8: 39.1: 514.33. Initially, the mixture of TEOS, ethanol, CTAB and water was stirred for 3 h followed by the addition of ammonia. Afterwards, it was continuously stirred and heated to 70 °C for 9 h. As obtained white product was centrifuged at 5000 rpm for 10 min and washed several times with ethanol and water. This solid product is named as as-synthesized silica (AS).

2.2. Synthesis of Etched SiO_2

Firstly, AS (0.3 g) is dispersed in 150 ml water and then it was further ultrasonically dispersed with 0.29 g of PVP (polyvinylpyrrolidone) in 15 ml of water. To this solution, 0.6g etchant NaBH_4 (sodium borohydride) was added under vigorous stirring at 56°C for 5 hrs. After etching, product etched silica (ES) was washed using centrifugation and was further calcined in air at 550°C for 5 h for effective removal of CTAB [51]. The resultant product is named as etched calcined silica (ECS). The overall procedure is schematically shown in Fig. 1.

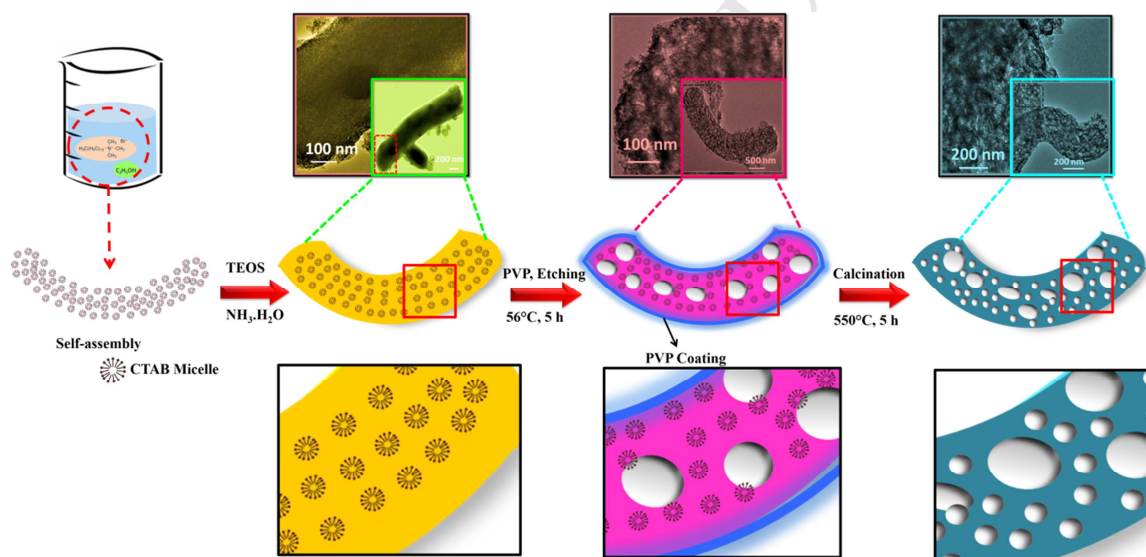


Fig. 1. Schematic showing the procedure involved in the synthesis of etched-calcined silica (ECS).

2.3. Characterisation

Structural framework of the powder sample was analysed using a BRUKER, TENSOR 27 FTIR spectrometer. X-ray diffraction pattern was recorded (2 to 80°) using XRD BRUKER D8 advance with $\text{Cu } k_\alpha$ 1.54 \AA . Raman spectra was measured on RENISHAW INVIA REFLEX MICRO-RAMAN spectrometer. The surface composition was estimated by Thermo Gravimetric Analysis (LINSEIS for air and PERKIN-ELMER for

nitrogen) and X-ray photoelectron spectroscopy (XPS, AXIS ULTRA 165 with C 1s peak at 284.8 used as standard). The overall composition was evaluated by EDAX (Energy Dispersive Spectroscopy). The band gap was determined using Tauc plot via optical (UV-Vis, UV-2600 SHIMADZU) spectrophotometer. Conductivity measurement was carried out at Keithley 4200-SCS at room temperature. Surface area was examined by BET technique (Quantachrome ASiQwin). High resolution transmission electron microscopy (HRTEM, Phillips Technai T-300 microscope) and field-emission scanning electron microscope (FESEM, ZEISS GEMINI) were employed to study the morphological feature of the samples. Cyclic Voltammetry (CV) at different scan rates and Electrochemical Impedance spectroscopy (EIS) was carried out in the frequency range of 10 mHz-100 kHz by CHI 604D electrochemical analyzer. Galvanostatic Charge-Discharge (GCD) and cycling measurements were recorded using Potentiostat Galvanostat EIS Analyzer PARSTAT 4000.

2.4. Cell Fabrication

3.0 mg of ECS (20 % acetylene black) was ultrasonically dispersed with 3 μ L of Nafion binder in isopropyl alcohol. This mixture was deposited onto 1.0 cm^2 area of the polished graphite sheet and was dried overnight at 80 $^\circ\text{C}$. Mass loading was found to be 0.7 mg cm^{-2} . ECS||ECS cell was fabricated by sandwiching an ion conducting separator membrane between two electrodes.

3. Results and discussion

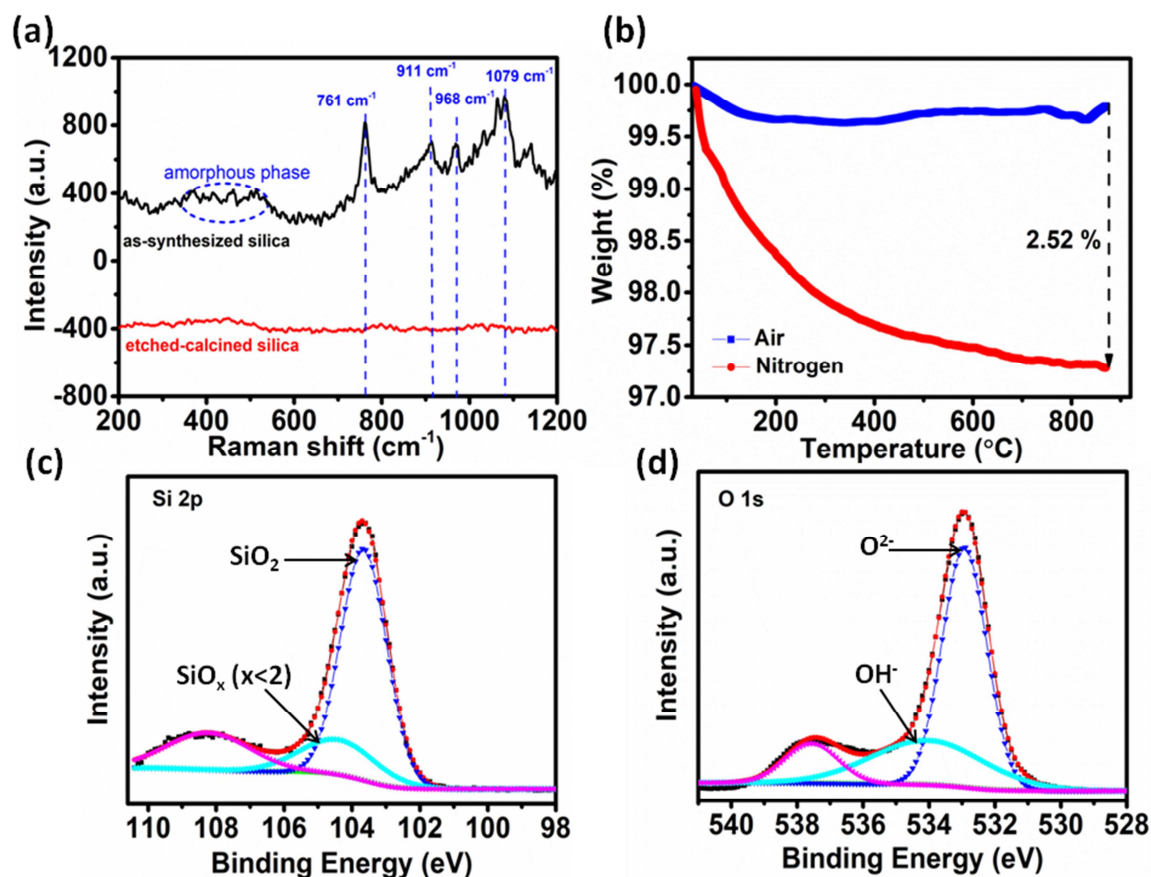


Fig. 2. Structure and compositional analysis of silica: (a) Raman spectra of AS and ECS. (b) TGA analysis of ECS in air and nitrogen. (c) XPS spectra of Si 2p (ECS). (d) XPS spectra of O 1s (ECS).

Fig. 2a shows the characteristic Raman peaks of silica [52–54]. Raman spectra of the ECS shows broadened peaks as compared to the AS. It is known that phonon confinement effect (if crystallite grain size < 10 nm) and change in oxygen stoichiometry are responsible for the peak broadening and red shift of Raman spectra [55]. Here, the possibility of phonon confinement is ruled out as the size of grain is larger than 10 nm (supported by TEM results (Fig. S1)). Therefore, the above observation is directing towards the existence of oxygen vacancies (OVs). In order to ensure the oxygen vacancies (OVs), TGA in Fig. 2b is analysed. ECS thermograms in air and Nitrogen ambient confirm the presence of oxygen vacancies. It is observed that there is a less weight loss in air as compared to nitrogen. Approximately

17.25 % oxygen vacancy is concluded from TGA analysis that warrants the change in composition from SiO_2 to $\text{SiO}_{1.65}$. Si 2p XPS spectra (Fig. 2c) of ECS with peak at about 104.4 eV also suggest the change in composition of SiO_2 [15]. The O 1s (Fig. 2d) binding energies 532.93 eV, 534.04 eV and 537.56 represent O^{2-} , OH^- and chemisorbed water respectively [56]. The calculated surface composition of the ECS from XPS is $\text{SiO}_{1.69}$ changes from $\text{SiO}_{2.19}$ of AS (Table. S1). Both TGA and XPS results are close to each other and hence confirming the compositional change in silica. Further amorphous nature and structural framework of silica is also confirmed by FTIR and XRD analysis (Fig. S2a and b).

FESEM micrographs in (Fig. 3a, b and c) depict cashew nut shaped morphology of as-synthesized silica (AS), etched silica (ES) and etched-calcined silica (ECS) respectively.

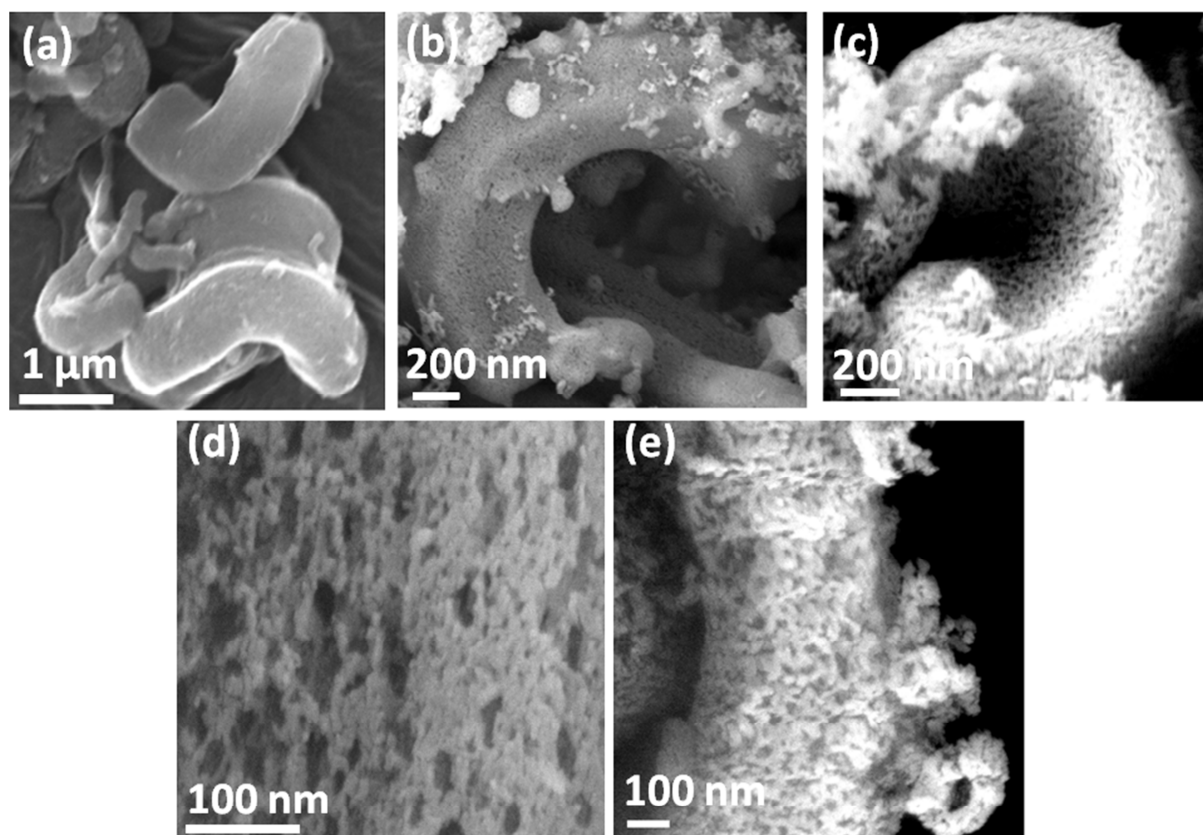


Fig. 3. FESEM micrographs of silica: (a) as-synthesized silica (AS). (b & d) etched silica (ES). (c & e) etched-calcined silica (ECS).

Fig. 3d, high resolution FESEM micrograph of ES illustrates the surface roughness on the cashew nut shaped structure after etching treatment. During etching process, reduction occurs and creates oxygen vacancies (OVs) that perturb the arrangement of Si-O units on the surface [57] leading to a defected surface. After calcination, some small pores are also generated (Fig. 3e) which results in an overall bimodal mesoporous structure with oxygen vacant sites at the surface of ECS. This defect induced surface with abundant oxygen vacancies (OVs) behaves as a quantum well in which the electron hopping take place [58].

TEM micrographs (Fig. 4a) of AS depicts that the SiO_2 particles as seen in FESEM are $\sim 2\mu\text{m}$ in length. The high resolution TEM micrograph of AS in Fig. 4b suggests that there is a negligible/inaccessible porosity. After etching with NaBH_4 , the TEM micrograph of ES (Fig. 4c) reveals rough surface owing to the regrowth of silica. Zhang *et al.* 2009 [43] proposed that two separate processes are involved in etching, one is dissolution of SiO_2 owing to high basicity of NaBH_4 solution and other is regrowth of silica on increasing concentration of BO_2^- ions (released on reaction of NaBH_4 with water). Retention of surface morphology even after etching process is due to the PVP which serves as a support to preserve morphology. The role of PVP molecule is to block the outward dissolution of silicate [59].

TEM findings (Fig. 4d) indicate occurrence of strong chemical etching that creates surface defects resulting in pores. Pores of ~ 12 nm are evidently seen at the surface of etched cashew nut structures. Etching not only introduces mesopores in the structure but also alter the surface stoichiometry of oxygen. Post etching calcination treatment decorated the morphology with smaller pores of dia. 6-7 nm, which are clearly visible in the TEM micrograph of ECS (Fig. 4e and f). Successive etching and calcination treatments resulted in bimodal porosity and oxygen vacancy in silica particles without affecting their size and shape. TEM micrographs suggest that the pores are interconnected and form channels to

provide swift passage to the ionic charges and electronic transfer [60]. TEM and FESEM results are further confirmed by BET measurement (Fig. S3a and b) which proves the existence of bimodal mesoporous structure with high BET surface area $\sim 878 \text{ m}^2 \text{ g}^{-1}$.

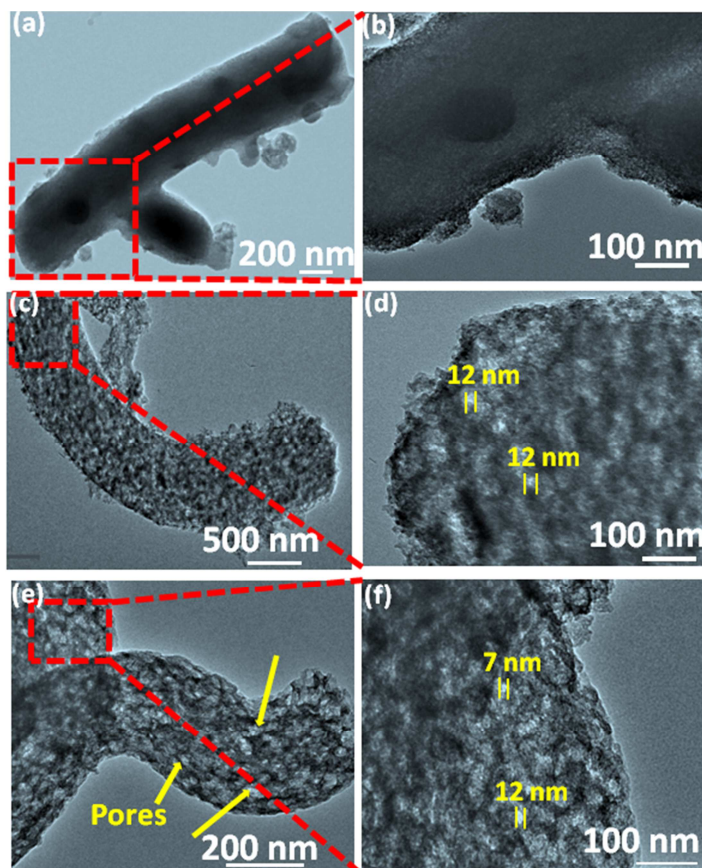


Fig. 4. TEM micrographs of silica: (a & b) as-synthesized silica (AS). (c & d) etched silica (ES). (e & f) etched-calcined silica (ECS).

The electrochemical performance of silica electrodes was studied using a three-electrode cell in 1.0 M H_2SO_4 electrolyte, with Ag/AgCl as the reference and Pt as the counter electrodes, respectively. Fig. 5a shows the voltammograms of AS, ES and ECS measured at 5 mV s^{-1} . Enclosed area in the voltammogram obtained from ECS working electrode is greater than ES and AS. The large area under the voltammetric loop i.e. high charge storage in ECS demonstrate the combined advantages of bimodal porosity and oxygen vacancies into the structure. These results display ECS as best performer among these electrodes (AS, ES and ECS) for charge storage. Nyquist plot in Fig. 5b, suggests that the

ECS electrode is more capacitive compared to other electrodes whereas, Bode angle of ECS (inset Fig. 5b) is slightly larger than ES. To further understand the reason of more capacitive nature of ECS electrode, Mott–Schottky plot (C^{-2} vs. V , where $C = -1/2\pi fZ''$) was analysed at a frequency of 10 kHz. In Fig. 5c, ECS electrode shows the positive slope indicating the n–type dopant. The slope of Mott–Schottky plot is used to estimate the carrier/donor densities using equation [61].

$$N_d = \left(\frac{2}{e_0 \varepsilon \varepsilon_0} \right) \left[\frac{d\left(\frac{1}{C^2}\right)}{dV} \right]^{-1} \quad (1)$$

Where, N_d is the carrier concentration or donor density, e_0 charge of electron, ε is the dielectric constant of SiO_2 (3.9) [62], ε_0 is permittivity of vacuum, C is the capacitance and V is the applied potential. The carrier/donor density calculated from the above equation is $3.0 \times 10^{24} \text{ cm}^{-3}$ for ECS suggest good electronic conductivity, since the electrical conductivity is directly depends on the carrier/donor density [63]. As the donor density increases, current density should also increase because the tunnelling probability of electron increases. Tunnelling probability depends on the distance between the active sites and this distance can be calculated from the expression:

$$d = \frac{1}{N_d^{1/3}} \quad (2)$$

To calculate the distance between active site in the thin film of geometrical area 1 cm^2 , the actual thickness of film 2000 \AA is also considered. Therefore, for this the carrier density calculated is $6 \times 10^{19} \text{ cm}^{-3}$ and distance between the active sites is estimated to be 2.5 nm that is much less hence escalating the rate capability [58]. Rate of electron transfer also enhances as it is an exponentially decreasing function of tunnelling distance [58]. To discover the impact of OV's on the band gap of ECS, UV-vis spectra (Fig. 5d) is recorded. The direct band gap energy for ECS is reduced to 2.1 eV compared to the previously reported value [64] for SiO_2 due to the generation of defect related energy levels as well as the bimodal mesoporous

structure. Hence, it can be inferred that oxygen vacancies not only improves the rate of electron transfer but also contribute to the conductivity of ECS electrode via reducing the band gap.

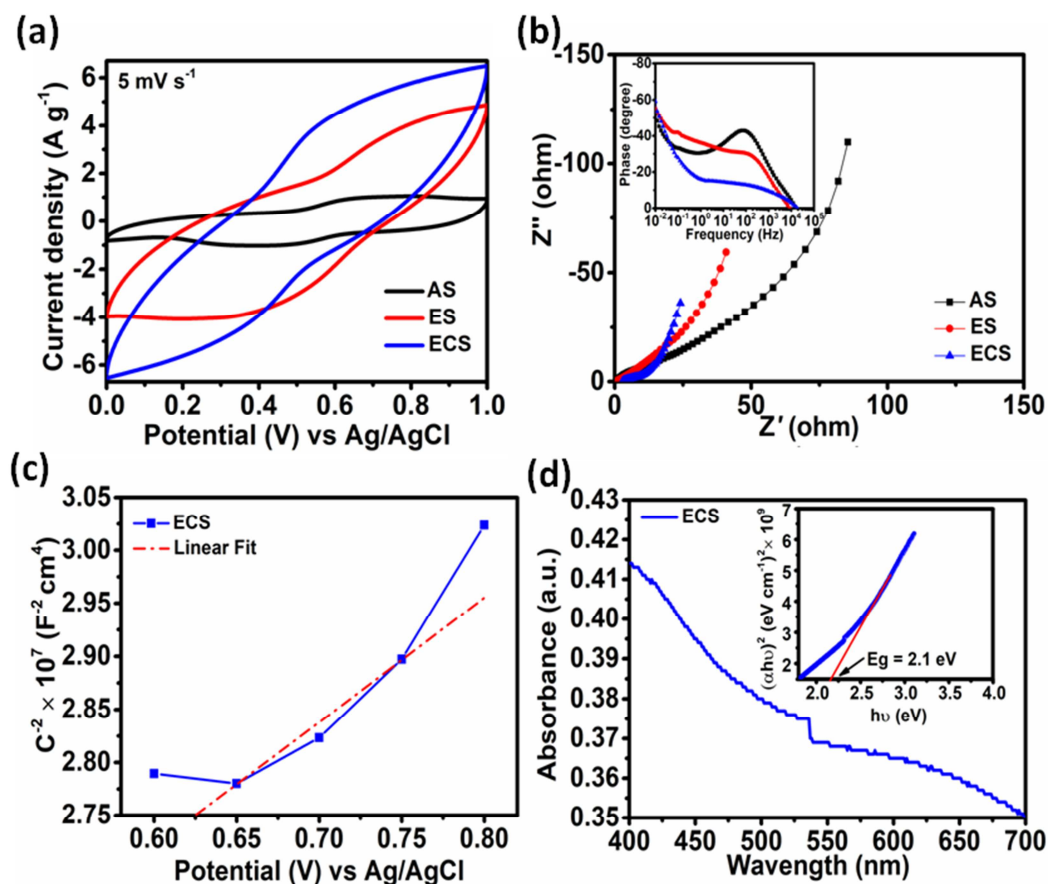


Fig. 5. (a) Cyclic voltammograms of AS, ES and ECS. (b) Nyquist plot of AS, ES and ECS (inset shows Bode plot). (c) Mott–Schottky plot of ECS. (d) UV-visible spectra (the inset displays Tauc plot) of ECS.

To evaluate the synergistic effect of bimodal porosity and oxygen vacancies over ECS electrode, electrochemical measurements were carried out. Fig. S4a shows the voltammogram of ECS electrode at different scan rates. The specific capacitance calculated at 5 mV s^{-1} in Fig. S4b (Supporting Information) show a high value of charge stored (705.0 F g^{-1}). Furthermore, the ECS electrode demonstrates an excellent cyclic stability with more than 112 % retention after 5000 cycles due to the high carrier concentration that improves the rate capability (Fig. S5).

To further understand the dependence of charge storage on scan rate, Trasatti plot is analysed [65,66]. According to Trasatti, the total charge stored (q_t) is the sum of the contribution of charge provided by inner (q_i) and outer surface (q_o) of the electrode. Due to the faster kinetics, the amount of charge stored in the outer surface is diffusion limited and it is calculated by linear fit of q^* vs $v^{-1/2}$ when the scan rate i.e. $v = \infty$ (Fig. 6a). Similarly, the total charge stored is evaluated by making linear fit in the curve of $1/q^*$ vs $v^{1/2}$ at $v = 0$ (Fig. 6b) as here diffusion of ion is unlimited. The obtained charge at the outer surface (q_o) is 59.47 C g^{-1} and the total amount of charge stored (q_t) is 227 C g^{-1} . The value obtained for q_o/q_t (25.99) illustrate higher inner active surface contribution compared to outer active surface due to high ionic mobility and swift pathway for charge carriers in the wide mesopores.

In order to identify the mechanism behind the charge stored in ECS electrode, kinetics of charge storage at different potential is studied. Commonly, the total amount of charge stored originates from intercalation/de-intercalation and capacitive mechanism [67]. This is characterised by studying the cyclic voltammogram at different scan rates using Power's law [68].

$$i(V) = av^b \quad (3)$$

Here, a and b are the adjustable parameters and v is the scan rate (V s^{-1}). Value of b can be determined from the slope of $\log i$ vs $\log v$. There are two conditions i.e. for $b = 0.5$ major contribution arises from intercalation/de-intercalation of ions However, for $b = 1$ capacitive process dominates. Fig. 6c illustrates the plot of $\log i$ vs $\log v$ at different potential and depicts the value of b closer to 0.5 at each potential (Fig. 6d). This elaborates charge storage mechanism in ECS is intercalation/de-intercalation (charge storage is diffusive). Large mesopores of 10 to 18 nm are suitable for the intercalation mechanism. They offer large surface area and in turn decrease the current density per unit surface area i.e. reducing the electrode polarization and improving charge transfer [69].

The current contribution from capacitive and intercalation mechanism can be determined using the following equation [70].

$$i(V) = k_1(\vartheta) + k_2(\vartheta)^{\frac{1}{2}} \quad (4)$$

Plotting the $i(V)/v^{1/2}$ vs $v^{1/2}$ determines k_1 and k_2 at each fixed potential. The value of $k_1(v)$ and $k_2(v)^{1/2}$ corresponds to current contribution from capacitive and diffusion controlled intercalation mechanism respectively. At lower scan rates contribution from intercalation is maximum whereas on further increasing the scan rate intercalative contribution decreases leading to the enhancement in capacitive current (inset Fig. 6d).

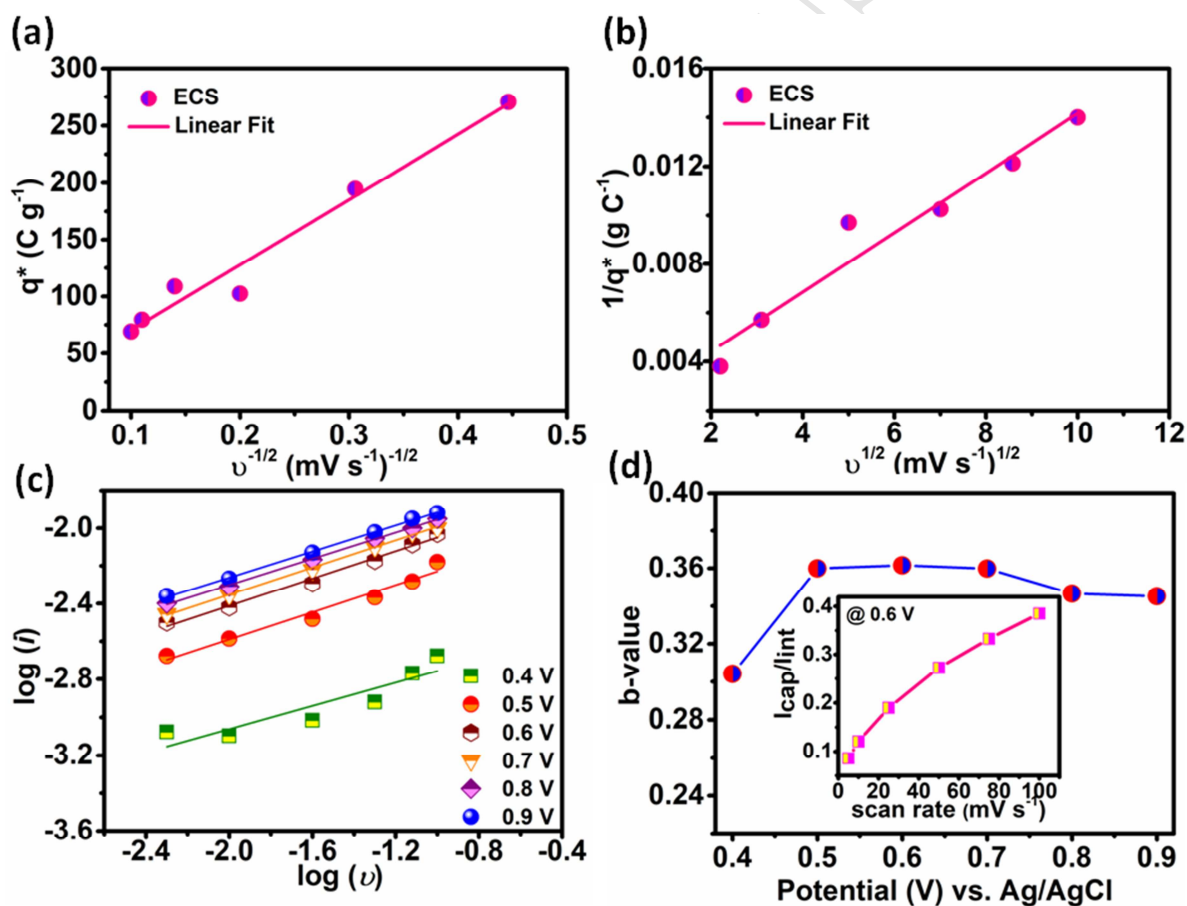


Fig. 6. (a & b) Trasatti plot of ECS. (c) Plot of $\log(i)$ vs $\log(v)$ at different potentials. (d) dependence of slope 'b' as a function of different potentials (the inset shows variation of I_{cap}/I_{int} with different scan rate at 0.6 V).

Intercept of high frequency Nyquist plot (Fig. S6a) on the real axis depicts the magnitude of solution resistance (R_s) of 2.9 Ω (inset Fig. S6a) [71]. The smaller value of R_s is due to the good contact between electrode and electrolyte owed to the high surface area. In the Bode plot, observed phase angle for ECS $\sim -59^\circ$ (Fig. S6b) at 0.01 Hz suggest effective ion diffusion in mesopores at mid frequency region. This deviation from ideal capacitive behaviour is attributed to broad pore size distribution in mesoporous range. At the same frequency, penetration of *ac* signal varies for different pore dimensions. This leads to frequency dispersion in which low frequency impedance behaviour is shifted from the theoretical vertical line [72,73].

Specific capacitance increases considerably with a decrease in the frequency at the low-frequency region (inset Fig. S6b). From this capacitance value, electrochemically active surface area i.e. the accessible surface area of the electrode is estimated to be 3170 $\text{m}^2 \text{g}^{-1}$ which is much higher than the BET surface area. This large difference is ascribed to the reason that the BET measurement does not include interlayer surface area. Specifically, the availability of this high electrochemical surface area with less effective distance for electrolytic ion and electron transport is favourable for intercalation of electrolytic ions.

A shorter Warburg region (17.78 Hz-3.61 Hz) (Figure S6a Supporting Information) corresponds to high ionic diffusion in ECS [74]. Ionic diffusion can be evaluated from the plot of real part of impedance and reciprocal root square of lower angle frequency shows a straight line (Figure S6c Supporting Information).

High value of diffusion coefficient ($1.05 \times 10^{-9} \text{ cm}^2 \text{ s}^{-1}$) validates less inhibition in movement of ions across the wider pores that are estimated by the BJH adsorption value of average pore diameter of 7.4 nm. The credit for high ionic mobility goes to internal voids and reduced tunnelling distance between the active sites.

GCD measurements (Fig. 7a) of ECS||ECS cell are performed at increasing current densities. The GCD characteristics demonstrate isosceles triangular shape indicating nearly identical charge and discharge. The slight deviation from isosceles triangular character is due to the contribution from surface redox reaction of hydroxyl group [21]. The specific capacitance is evaluated from GCD measurements and found to be 337.0, 218.0, 142.0, 98.0, 70.0 and 52.0 F g⁻¹ at current density of 1.0, 2.0, 3.0, 4.0, 5.0 and 6.0 A g⁻¹ respectively. High capacitance with low ESR of 0.05 Ω (inset Fig. 7a) indicates towards the less consumption of energy during charging/discharging [75].

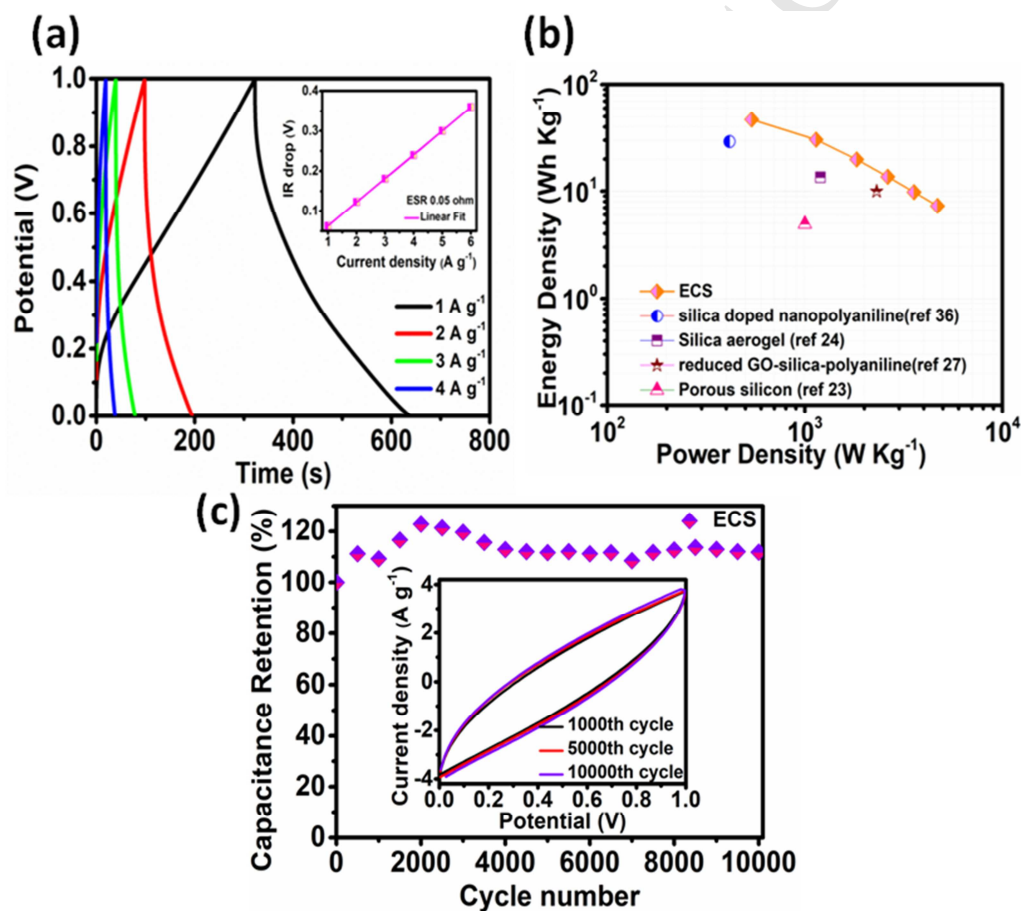


Fig. 7. (a) Galvanostatic charge/discharge measurement of ECS||ECS (inset shows plot of IR drop vs. current density). (b) Ragone plot of ECS||ECS with literature reported values. (c) Cyclic stability of ECS||ECS at 100 mV s⁻¹.

Etchant NaBH_4 reduces few of silica to silicon thus boost the conductivity without removing SiO_2 core [76]. This lowers the density of silica and thus increases specific capacitance of unit mass. The gravimetric capacitance of ECS is relatively high compared to previously reported values for porous silica and silicon [22–26].

Fig. 7b, illustrates the performance of the ECS||ECS cell. It is inferred that ECS possess a high energy density of 46.86 Wh Kg^{-1} at 537.59 W Kg^{-1} at a current density of 1 A g^{-1} . Fig. 7c, shows 111 % of capacitance retention upto 10000 cycles. This implies, ECS is an excellent material for supercapacitor device. The reason behind this appreciable cycle stability may be mesoporous structure with hydrophilic surface functionality as it allows the wettability of the electrode/electrolyte interface and also the large number of carriers that enhances the rate of transfer of electron. Considering the specific capacitance and energy density, the performance of present work is compared with the other silica based electrodes and electrolyte membrane in Table 1.

Table 1.

Electrode	Electrolyte	Specific Capacitance (F g^{-1})	Energy density	Reference
Graphene coated Porous silicon	1-ethyl-3-methylimidazolium tetrafluoroborate (EMIBF_4)	-	$4.8\text{-}4.9 \text{ Wh Kg}^{-1}$ at 1000 W Kg^{-1}	23
SiO_2 aerogel	1 M $\text{Et}_4\text{NBF}_4/\text{PC}$	62.5 F g^{-1}	13.5 Wh Kg^{-1} at 1200 W Kg^{-1}	24
Reduced graphene oxide-silica in polyaniline	1 M H_2SO_4	318 F g^{-1}	17 Wh Kg^{-1} at 100 W Kg^{-1}	27
10% silica doped nanopolyaniline	1 M H_2SO_4	368 F g^{-1}	37.4 Wh Kg^{-1} at 430 W Kg^{-1}	36
Stainless steel foil	silicotungstic acid(SiWA)- H_3PO_4 -PVA/ SiO_2	$23 \mu\text{F cm}^{-2}$	-	77

SiO ₂ @C/TiO ₂	1 M KOH	1018 F g ⁻¹	-	78
MWCNT	SiO ₂ , PVDF and imidazolium ionic liquid	71.7 F g ⁻¹	32.2 Wh Kg ⁻¹ at 900 W Kg ⁻¹	79
Oxygen deficient, bimodal mesoporous silica	1 M H ₂ SO ₄	337 F g ⁻¹	46.86 Wh Kg ⁻¹ at 537.59 W Kg ⁻¹	(This work)

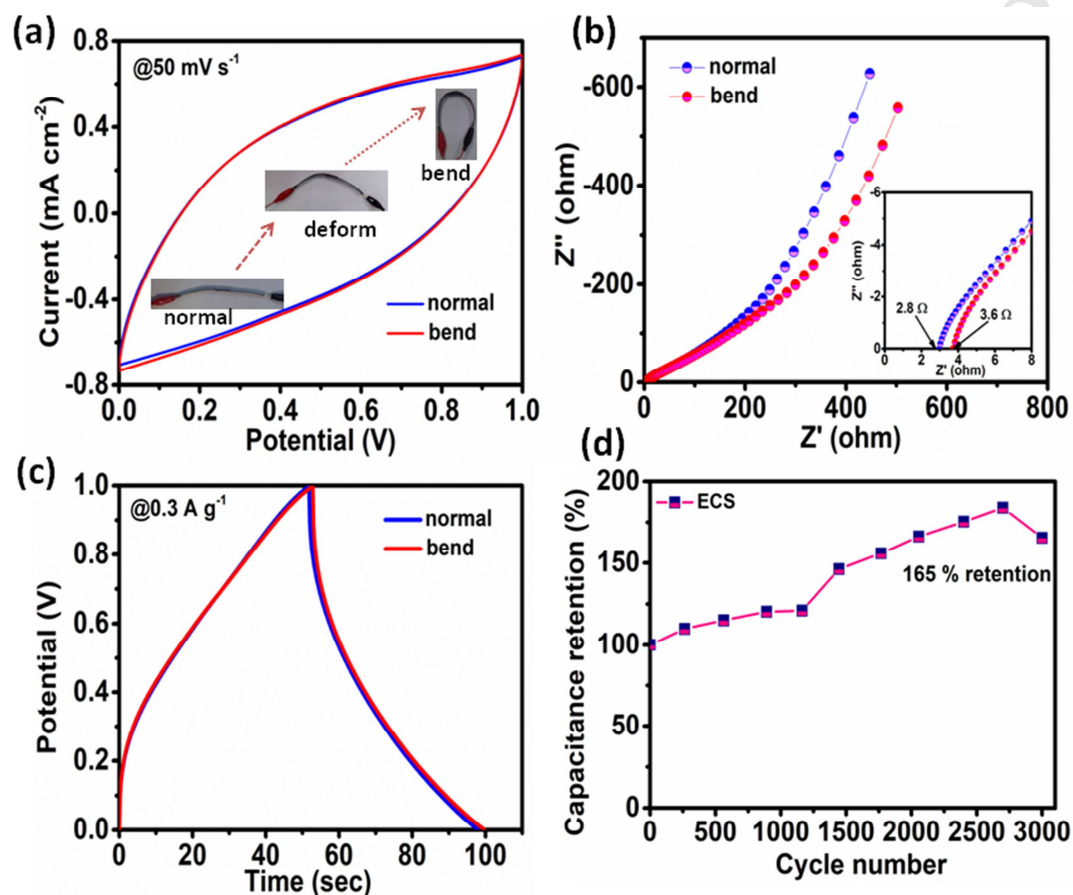


Fig. 8. Electrochemical performance of flexible solid state ECS||ECS device: (a) Cyclic voltammograms. (b) Nyquist plot. (c) Galvanostatic charge/discharge characteristics. (d) Cycling stability at 100 mV s⁻¹.

To broaden the utility of ECS||ECS device, we have fabricated flexible solid state symmetric device using active area of 1cm × 1cm with PVA/H₂SO₄ [80] (gel electrolyte) and flexible graphite (substrate). Fig. 8a shows the comparison of CV voltammogram under normal and bend conditions, revealing no change in the shape of curve that confirms the structural

integrity of the device. Further, Nyquist plot (Fig. 8b) shows slight influence of mechanical deformation on the device with a minimal increase of solution resistance. However, in both normal and bent conditions straight line nearly parallel to imaginary axis depicts good capacitive behaviour of the device. GCD characteristics in Fig. 8c demonstrate the similar charge discharge behaviour in both conditions. It can be clearly seen that mechanical distortion has no major effect on capacitive performance of the device and shows an energy density of 2.16 Wh Kg^{-1} at power density of 0.16 KW Kg^{-1} comparable to other solid state devices [81–83]. Cycle life is another parameter to evaluate the performance of device. Interestingly, solid state flexible device shows capacitance retention of 165% after 3000 cycles (Fig. 8d) indicating excellent stability of device. The high mechanical and electrical strength is attributed to the interconnected mesoporous structure and abundant oxygen vacancies.

4. Conclusions

In summary, the etched-calcined silica (ECS) enriched with abundant oxygen vacant sites and mesopores is employed as a charge storage material. ECS along with oxygen vacant sites acquires large electrochemically active surface area ($3170 \text{ m}^2 \text{ g}^{-1}$) to ensure the maximum utilization. These oxygen vacant sites with distinguishable interconnected pores provide less inhibition in diffusion of electrolytic ions by enlarging the electrode/electrolyte interfacial area. Oxygen vacancies (OVs) in silica ameliorate the rate of electron transfer and decrease the band gap by increasing the carrier concentration ($3 \times 10^{24} \text{ cm}^{-3}$) and reducing the distance between active sites (2.5 nm). The oxygen deficient ECS cell shows a high performance of 337 F g^{-1} at 1 A g^{-1} that is mainly attributed to bimodal mesoporosity and the high concentration of carriers. In addition, more than 110% capacitance is retained up to 10000 cycles that are mainly attributed to the mesoporous structure. Furthermore, solid state performance of flexible device of silica

elucidated it as an excellent material for portable and flexible electronic device. Hence, this work proposes a wise strategy to make silica based materials capacitive by introducing OV's and simultaneously inculcating bimodal mesopores in the structure. This study might lead to further progress in research of silica as a charge storage material.

Conflicts of interest

There are no conflicts to declare.

Acknowledgements

Akanksha Joshi is grateful to Junior Research Fellowship award (09/045 (1422)/2016-EMR-I) from Council of scientific industrial research (CSIR), India. Shubra Lalwani also acknowledges CSIR India for award of Senior Research fellowship (09/045/(1365)/2015-EMR-I).

References

- [1] H. Wang, H. Dai, Strongly coupled inorganic-nano-carbon hybrid materials for energy storage, *Chem. Soc. Rev.* 42 (2013) 3088–3113.
- [2] E.A. Rosa, T. Dietz, T. Human drivers of national greenhouse-gas emissions, *Nature Clim. Change* 2 (2012) 581–586.
- [3] A. Nozad Golikand, M. Bagherzadeh, Z. Shirazi, Evaluation of the Polyaniline Based Nanocomposite Modified with Graphene Nanosheet, Carbon Nanotube, and Pt Nanoparticle as a Material for Supercapacitor, *Electrochimica Acta* 247 (2017) 116–124.
- [4] N. Padmanathan, S. Selladurai, K.M. Razeeb, Ultra-fast rate capability of a symmetric supercapacitor with a hierarchical Co_3O_4 nanowire/nanoflower hybrid structure in nonaqueous electrolyte, *RSC Adv.* 5 (2015) 12700–12709.

- [5] A. N. Naveen, S. Selladurai, Novel low temperature synthesis and electrochemical characterization of mesoporous nickel cobaltite-reduced graphene oxide (RGO) composite for supercapacitor application, *Electrochimica Acta* 173 (2015) 290–301.
- [6] J. Zhu, Y. Xu, J. Hu, L. Wei, J. Liu, M. Zheng, Facile synthesis of MnO₂ grown on nitrogen-doped carbon nanotubes for asymmetric supercapacitors with enhanced electrochemical performance, *J. Power Sources* 393 (2018) 135–144.
- [7] T. Alamro, M. K. Ram, Polyethylenedioxythiophene and molybdenum disulfide nanocomposite electrodes for supercapacitor applications, *Electrochimica Acta* 235 (2017) 623–631.
- [8] V. Sahu, S. Shekhar, P. Ahuja, G. Gupta, S.K. Singh, R.K. Sharma, G. Singh, Synthesis of hydrophilic carbon black; role of hydrophilicity in maintaining the hydration level and protonic conduction, *RSC Adv.* 3 (2013) 3917–3924.
- [9] V. Sahu, M. Mishra, G. Gupta, G. Singh, R.K. Sharma, Turning Hazardous Diesel Soot into High Performance Carbon/MnO₂ Supercapacitive Energy Storage Material, *ACS Sustainable Chem. Eng.* 5 (2017) 450–459.
- [10] H. Sun, Y. Zhao, K. Mølhave, M. Zhang, J. Zhang, Simultaneous modulation of surface composition, oxygen vacancies and assembly in hierarchical Co₃O₄ mesoporous nanostructures for lithium storage and electrocatalytic oxygen evolution, *Nanoscale* 9 (2017) 14431–14441.
- [11] Y. Cui, C.M. Lieber, Functional Nanoscale Electronic Devices Assembled Using Silicon Nanowire Building Blocks, *Science* 291 (2001) 851–853.
- [12] S. Cao, Z. Zhao, X. Jin, W. Sheng, S. Li, Y. Ge, M. Dong, W. Wu, L. Fang, Unique double-shelled hollow silica microspheres: template-guided self-assembly, tunable pore

- size, high thermal stability, and their application in removal of neutral red, *J. Mater. Chem.* 21 (2011) 19124–19131.
- [13] L. Zhang, S.Z. Qiao, Y.G. Jin, Z.G. Chen, H.C. Gu, G.Q. Lu, Magnetic Hollow Spheres of Periodic Mesoporous Organosilica and Fe₃O₄ Nanocrystals: Fabrication and Structure Control, *Adv. Mater.* 20 (2008) 805–809.
- [14] S.Y. Kim, B.H. Kim, Silica decorated on porous activated carbon nanofiber composites for high-performance supercapacitors, *J. Power Sources* 328 (2016) 219–227.
- [15] P.C. Carman, Constitution of colloidal silica, *Trans. Faraday Soc.* 36 (1940) 964–973.
- [16] H. Peng, M. Jain, D.E. Peterson, Y. Zhu, Q. Jia, Composite Carbon Nanotube/Silica Fibers with Improved Mechanical Strengths and Electrical Conductivities, *Small* 2008, 4, 1964–1967.
- [17] A. Magasinski, P. Dixon, B. Hertzberg, A. Kvit, J. Ayala, G. Yushin, High-performance lithium-ion anodes using a hierarchical bottom-up approach, *Nat. Mater.* 9 (2010) 353–358.
- [18] H. Kim, M. Seo, M.H. Park, J. Cho, A Critical Size of Silicon Nano□Anodes for Lithium Rechargeable Batteries, *Angew. Chem. Int. Ed.* 49 (2010) 2146–2149.
- [19] Q. Liu, Z. Cui, R. Zou, J. Zhang, K. Xu, J. Hu, Surface Coating Constraint Induced Anisotropic Swelling of Silicon in Si–Void@SiO_x Nanowire Anode for Lithium□Ion Batteries, *Small* 13 (2017) 1603754.
- [20] M.P. Liu, C.H. Li, H.B. Du, X.Z. You, Facile preparation of silicon hollow spheres and their use in electrochemical capacitive energy storage, *Chem. Commun.* 48 (2012) 4950–4952.
- [21] J.F. Wang, K.X. Wang, F.H. Du, X.X. Guo, Y.M. Jiang, J.S. Chen, Amorphous silicon with high specific surface area prepared by a sodiothermic reduction method for supercapacitors, *Chem. Commun.* 49 (2013) 5007–5009.

- [22] S.E. Rowlands, R.J. Lantham, W.S. Schlindwein, Supercapacitor devices using porous silicon electrodes, *Ionics* 5 (1999) 144–149.
- [23] L. Oakes, A. Westover, J.W. Mares, S. Chatterjee, W.R. Erwin, R. Bardhan, S.M. Weiss, C.L. Pint, Surface engineered porous silicon for stable, high performance electrochemical supercapacitors, *Scientific Reports* 3 (2013) 3020 DOI :10.1038/srep03020.
- [24] X. Du, C. Wang, T. Li, M. Chen, Studies on the performances of silica aerogel electrodes for the application of supercapacitor, *Ionics* 15 (2009) 561–565.
- [25] G.H. Jeong, H.M. Lee, J.G. Kang, H. Lee, C.K. Kim, J.H. Lee, J.H. Kim, S.W. Kim, ZrO₂–SiO₂ Nanosheets with Ultrasmall WO₃ Nanoparticles and Their Enhanced Pseudocapacitance and Stability, *ACS Appl. Mater. Interfaces* 6 (2014) 20171–20178.
- [26] J. Zhi, S. Deng, Y. Wang, A. Hu, Highly Ordered Metal Oxide Nanorods inside Mesoporous Silica Supported Carbon Nanomembranes: High Performance Electrode Materials for Symmetrical Supercapacitor Devices, *J. Phys. Chem. C* 119 (2015) 8530–8536.
- [27] U. Male, S. Uppugalla, P. Srinivasan, Effect of reduced graphene oxide–silica composite in polyaniline: electrode material for high-performance supercapacitor, *J. Solid State Electrochem.* 19 (2015) 3381– 3388.
- [28] J. Zhao, Y. Zhang, T. Wang, P. Li, C. Wei, H. Pang, Reed Leaves as a Sustainable Silica Source for 3D Mesoporous Nickel (Cobalt) Silicate Architectures Assembled into Ultrathin Nanoflakes for High Performance Supercapacitors, *Adv. Mater. Interfaces* 2 (2015) 1400377 DOI: 10.1002/admi.201400377.
- [29] M.H. Yu, H.N. Wang, X.F. Zhou, P. Yuan, C.Z. Yu, One Template Synthesis of Raspberry-like Hierarchical Siliceous Hollow Spheres, *J. Am. Chem. Soc.* 129 (2007) 14576–14577.

- [30] F. Caruso, R.A. Caruso, H. Möhwald, Nanoengineering of Inorganic and Hybrid Hollow Spheres by Colloidal Templating, *Science* 282 (1998) 1111–1114.
- [31] J. Liu, S.B. Hartono, Y.G. Jin, Z. Li, G.Q. Lu, S.Z. Qiao, A facile vesicle template route to multi-shelled mesoporous silica hollow nanospheres, *J. Mater. Chem.* 20 (2010) 4595–4601.
- [32] J.G. Wang, F. Li, H.J. Zhou, P.C. Sun, D.T. Ding, T.H. Chen, Silica Hollow Spheres with Ordered and Radially Oriented Amino-Functionalized Mesochannels, *Chem. Mater.* 21 (2009) 612–620.
- [33] V. Sahu, S. Shekhar, R.K. Sharma, G. Singh, Ultrahigh Performance Supercapacitor from Lacey Reduced Graphene Oxide Nanoribbons, *ACS Appl. Mater. Interfaces* 7 (2015) 3110–3116.
- [34] V. Sahu, S. Goel, R.K. Sharma, G. Singh, Zinc oxide nanoring embedded lacey graphene nanoribbons in symmetric/asymmetric electrochemical capacitive energy storage, *Nanoscale* 7 (2015) 20642–20651.
- [35] K.C. Leonard, W.E. Suyama, M.A. Anderson, Improvement of electrochemical capacitor electrodes using SiO₂ nanoparticles, *Electrochimica Acta* 56 (2011) 10137–10144.
- [36] H. Wei, H. Gu, J. Guo, S. Wei, J. Liu, Z. Guo, Silica Doped Nanopolyaniline with Endured Electrochemical Energy Storage and the Magnetic Field Effects, *J. Phys. Chem. C* 117 (2013) 13000–13010.
- [37] H. Jain, A. S. Nowick, Electrical conductivity of synthetic and natural quartz crystals, *J. Appl. Phys.* 53 (1982) 477.
- [38] S. Balendhran, J. Deng, J. Z. Ou, S. Walia, J. Scott, J. Tang, K.L. Wang, M.R. Field, S. Russo, S. Zhuiykov, M.S. Strano, N. Medhekar, S. Sriram, M. Bhaskaran, K.K. Zadeh,

- Enhanced Charge Carrier Mobility in Two-Dimensional High Dielectric Molybdenum Oxide, *Adv. Mater.* 25 (2013) 109–114.
- [39] H.S. Kim, J.B. Cook, H. Lin, J.S. Ko, S.H. Tolbert, V. Ozolins, B. Dunn, Oxygen vacancies enhance pseudocapacitive charge storage properties of MoO_{3-x} , *Nature Mater.* 16 (2016) 454–460.
- [40] D. Yan, W. Wang, X. Luo, C. Chen, Y. Zeng, Z. Zhu, NiCo_2O_4 with oxygen vacancies as better performance electrode material for supercapacitor, *Chem. Eng. Journal* 334 (2018) 864–872.
- [41] Y. Liu, C. Xiao, Z. Li, Y. Xie, Vacancy Engineering for Tuning Electron and Phonon Structures of Two-Dimensional Materials, *Adv. Energy Mater.* 6 (2016) 1600436.
- [42] D. Chen, L. Li, F. Tang, S. Qi, Facile and Scalable Synthesis of Tailored Silica “Nanorattle” Structures, *Adv. Mater.* 21 (2009) 3804–3807.
- [43] T. Zhang, Q. Zhang, J. Ge, J. Goe, M. Sun, Y. Yan, Y.S. Liu, C. Chang, J. Guo, Y. Yin, A Self-Templated Route to Hollow Silica Microspheres, *J. Phys. Chem. C* 113 (2009) 3168–3175.
- [44] Z.S. Wu, Y. Sun, Y.Z. Tan, S. Yang, X. Feng, K. Müllen, Three-Dimensional Graphene-Based Macro- and Mesoporous Frameworks for High-Performance Electrochemical Capacitive Energy Storage, *J. Am. Chem. Soc.* 134 (2012) 19532–19535.
- [45] Q. Zhang, L. Li, Y. Wang, Y. Chen, F. He, S. Gai, P. Yang, Uniform fibrous-structured hollow mesoporous carbon spheres for high-performance supercapacitor electrodes, *Electrochimica Acta* (176) 2015 542–547.
- [46] C.T. Hsu, C.C. Hu, Synthesis and characterization of mesoporous spinel NiCo_2O_4 using surfactant-assembled dispersion for asymmetric supercapacitors, *J. Power Sources* 242 (2013) 662–671

- [47] Z. Zheng, B. Huang, X. Meng, J. Wang, S. Wang, Z. Lou, Z. Wang, X. Qin, X. Zhang, Y. Dai, Metallic zinc- assisted synthesis of Ti^{3+} self-doped TiO_2 with tunable phase composition and visible-light photocatalytic activity, *Chem. Comm.* 49 (2013) 868–870.
- [48] W. Tian, Q. Gao, W. Qian, Interlinked Porous Carbon Nanoflakes Derived from Hydrolyzate Residue during Cellulosic Bioethanol Production for Ultrahigh-Rate Supercapacitors in Nonaqueous Electrolytes, *ACS Sustainable Chem. Eng.* 5 (2017) 1297–1305.
- [49] H. Cheng, M. Klapproth, A. Sagaltchik, S. Li, A. Thomas, Ordered mesoporous $\text{WO}_{2.83}$: selective reduction synthesis, exceptional localized surface plasmon resonance and enhanced hydrogen evolution reaction activity, *J. Mater. Chem. A* 6 (2018) 2249–2256.
- [50] S.A. Ansari, M.M. Khan, S. Kalathil, A. Nisar, J. Lee, M.H. Cho, Oxygen vacancy induced band gap narrowing of ZnO nanostructures by an electrochemically active biofilm, *Nanoscale* 5 (2013) 9238–9246.
- [51] X. Fang, C. Chen, Z. Liu, P. Liu, N. Zheng, A cationic surfactant assisted selective etching strategy to hollow mesoporous silica spheres, *Nanoscale* 3 (2011) 1632–1639.
- [52] F. Dai, J. Zai, R. Yi, M.L. Gordin, H. Sohn, S. Chen, D. Wang, Bottom-up synthesis of high surface area mesoporous crystalline silicon and evaluation of its hydrogen evolution performance, *Nature Communications* (2014) DOI: 10.1038/ncomms4605.
- [53] J. Mitra, M. Ghosh, R.K. Bordia, A. Sharma, Photoluminescent electrospun submicron fibers of hybrid organosiloxane and derived silica, *RSC Adv.* 3 (2013) 7591–7600.
- [54] L.Y. Yang, H.Z. Li, J. Liu, Z.Q. Sun, S.S. Tang, M. Lei, Dual yolk-shell structure of carbon and silica-coated silicon for high performance lithium-ion batteries, *Scientific Reports* DOI: 10.1038/srep10908.

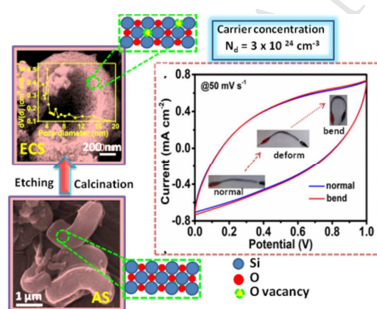
- [55] A. Naldoni, M. Allieta, S. Santangelo, M. Marelli, F. Fabbri, S. Cappelli, C.L. Bianchi, R. Psaro, V.D. Santo, Effect of Nature and Location of Defects on Bandgap Narrowing in Black TiO₂ Nanoparticles, *J. Am. Chem. Soc.* 134 (2012) 7600–7603.
- [56] E. McCafferty, J.P. Wightman, Determination of the concentration of surface hydroxyl groups on metal oxide films by a quantitative XPS method, *Surf. Interface Anal.* 26 (1998) 549–564.
- [57] Z. Sun, C. Yanga, G. Liu, H. Lua, R. Zhang, L. Wang, H. Wang, Largely enhanced electrochemical performance in MoO_{3-x} nanobelts formed by a “sauna reaction”: Importance of oxygen vacancies, *Electrochimica Acta* 239 (2017) 16–24.
- [58] B. Roh, D.D. Macdonald, Effect of oxygen vacancies in anodic titanium oxide films on the kinetics of the oxygen electrode reaction, *Russ. J. Electrochem.* 43 (2007) 125–135.
- [59] Q. Yu, J. Hui, P. Wang, X. Wang, Anion-Exchange-Driven Disassembly of a SiO₂/CTAB Composite Mesophase: the Formation of Hollow Mesoporous Silica Spheres, *Inorg. Chem.* 51 (2012) 9539–9543.
- [60] Z. Huang, Z. Zhang, X. Qi, X. Ren, G. Xu, P. Wan, X. Sun, H. Zhang, Wall-like hierarchical metal oxide nanosheet arrays grown on carbon cloth for excellent supercapacitor electrodes, *Nanoscale* 8 (2016) 13273–13279.
- [61] X. Lu, Y. Zeng, M. Yu, T. Zhai, C. Liang, S. Xie, M.S. Balogun, Y. Tong, Oxygen-Deficient Hematite Nanorods as High-Performance and Novel Negative Electrodes for Flexible Asymmetric Supercapacitors, *Adv. Mater.* 26 (2014) 3148–3155.
- [62] J. McPherson, J.Y. Kim, A. Shanware, H. Mogul, Thermochemical description of dielectric breakdown in high dielectric constant materials, *Appl. Phys. Lett.* 2003, 82, 2121.
- [63] X.Y. Cao, X. Xing, N. Zhang, H. Gao, M.Y. Zhang, Y.C. Shang, X.T. Zhang, Quantitative investigation on the effect of hydrogenation on the performance of

- MnO₂/H-TiO₂ composite electrodes for supercapacitors, *J. Mater. Chem. A* 3 (2015) 3785–3793.
- [64] T.H. DiStefano, D. Eastman, The band edge of amorphous SiO₂ by photoinjection and photoconductivity measurements, *Solid State Commun.* 9 (1971) 2259–2261.
- [65] S. Ardizzone, G. Fregonara, S. Trasatti, “Inner” and “outer” active surface of RuO₂ electrodes, *Electrochim. Acta* 35 (1990) 263–267.
- [66] R.K. Sharma, L. Zhai, Multiwall carbon nanotube supported poly(3,4-ethylenedioxythiophene)/manganese oxide nano-composite electrode for supercapacitors, *Electrochim. Acta* 54 (2009) 7148–7155.
- [67] B. Senthilkumar, K.V. Sankar, L. Vasylechko, Y.S. Lee, R.K. Selvan, Synthesis and electrochemical performances of maricite-NaMPO₄ (M = Ni, Co, Mn) electrodes for hybrid supercapacitors, *RSC Adv.* 4 (2014) 53192–53200.
- [68] K.V. Sankar, S. Surendran, K. Pandi, A.M. Allin, V.D. Nithya, Y.S. Lee, R.K. Selvan, Studies on the electrochemical intercalation/de-intercalation mechanism of NiMn₂O₄ for high stable pseudocapacitor electrodes, *RSC Adv.* 5 (2015) 27649–27656.
- [69] I. Moriguchi, R. Hidaka, H. Yamada, T. Kudo, H. Murakami, N.A. Nakashima, Nanocomposite of TiO₂ and Carbon Nanotubes as a High-Rate Li⁺-Intercalation Electrode Material, *Adv. Mater.* 18 (2006) 69–73.
- [70] M. Sathiyaraj, A.S. Prakash, K. Ramesh, J.M. Tarascon, A.K. Shukla, V₂O₅-Anchored Carbon Nanotubes for Enhanced Electrochemical Energy Storage, *Mesoporous, J. Am. Chem. Soc.* 133 (2011) 1629–16299.
- [71] H. Zhu, Y. Zheng, Mesoporous Co₃O₄ anchored on the graphitic carbon nitride for enhanced performance supercapacitor, *Electrochimica Acta* 265 (2018) 372–378.

- [72] J. Gamby, P.L. Taberna, P. Simon, J.F. Fauvarque, M. Chesneau, Studies and characterisations of various activated carbons used for carbon/carbon supercapacitors, *J. Power Sources* 101 (2001) 109–116.
- [73] H.K. Song, H.Y. Hwang, K.H. Lee, L.H. Dao, The effect of pore size distribution on the frequency dispersion of porous electrodes, *Electrochimica Acta* 45 (2000) 2241–2257.
- [74] H. Koga, H. Tonomura, M. Nogi, K. Suganuma, Y. Nishina, Fast, scalable, and eco-friendly fabrication of an energy storage paper electrode, *Green Chem.* 18 (2016) 1117.
- [75] Q. Wu, Y.X. Xu, Z.Y. Yao, A.R. Liu, G.Q. Shi, Supercapacitors Based on Flexible Graphene/Polyaniline Nanofiber Composite Films, *ACS Nano* 4 (2010) 1963–1970.
- [76] Z.Q. Zhang, C. Chen, C.C. Ma, M. Li, H. Chen, Z.G. Shang, Dependent Supercapacitive Characteristics of SiO₂/MnO₂ Core-shell Nanostructure, *Int. J. Electrochem. Sci.* 11 (2016) 6138–6148.
- [77] H. Gao, K. Lian, Effect of SiO₂ on Silicotungstic Acid-H₃PO₄-poly(vinyl alcohol) Electrolyte for Electrochemical Supercapacitors, *J. Electrochem. Soc.* 160 (2013) A505–A510.
- [78] Y. Zhang, Y. Zhao, S. Cao, Z. Yin, L. Cheng, L. Wu, Design and Synthesis of Hierarchical SiO₂@C/TiO₂ Hollow Spheres for High-Performance Supercapacitors, *ACS Appl. Mater. Interfaces* 9 (2017) 29982–29991.
- [79] P. Ortega, J. Trigueiro, G. Silva, R. Lavall, Improving supercapacitor capacitance by using a novel gel nanocomposite polymer electrolyte based on nanostructured SiO₂, PVDF and imidazolium ionic liquid, *Electrochimica Acta*, 188 (2015) 809–817.
- [80] S. Grover, S. Goel, R.B. Marichi, V. Sahu, G. Singh, R.K. Sharma, Polyaniline All Solid-State Pseudocapacitor: Role of Morphological Variations in Performance Evolution, *Electrochimica Acta* 196 (2016) 131–139.

- [81] Y. Xu, Z. Lin, X. Huang, Y. Liu, Y. Huang, X. Duan, Flexible Solid-State Supercapacitors Based on Three-Dimensional Graphene Hydrogel Films, *ACS Nano* 7 (2013) 4042–4049.
- [82] B.G. Choi, S.J. Chang, H.W. Kang, C.P. Park, H.J. Kim, W.H. Hong, S. Lee, Y.S. Huh, High performance of a solid-state flexible asymmetric supercapacitor based on graphene films, *Nanoscale* 4 (2012) 4983–4988.
- [83] Y.J. Kang, H. Chung, C.H. Han, W. Kim, All-solid-state flexible supercapacitors based on papers coated with carbon nanotubes and ionic-liquid-based gel electrolytes, *Nanotechnology* 23 (2012) 065401.

For Table of content only



Synergistic contribution of bimodal mesopores and oxygen vacancies in silica for excellent supercapacitive performance